

Design and Beam Test Results for the sPHENIX Electromagnetic Calorimeter Prototype

Abstract—sPHENIX is a future experiment at the Relativistic Heavy Ion Collider with the goal of studying the quark-gluon plasma and further understanding QCD matter and interactions. A prototype of the sPHENIX detector was tested at the Fermilab Test Beam Facility in Spring 2018 as experiment T-1044. The energy response of the EMCal was studied as a function of position and input energy. The resolution of the EMCal prototype was obtained after applying a position dependent correction (hodoscope-based or cluster-based) and a beam profile correction. The EMCal energy resolution was found to be $\sigma(E)/\langle E \rangle = 3.5(0.1) \oplus 13.3(0.2)/\sqrt{E}$ based on the hodoscope position dependent correction, and $\sigma(E)/\langle E \rangle = 3.0(0.1) \oplus 15.4(0.3)/\sqrt{E}$ based on the cluster position dependent correction. Both of these results meet the requirements of the sPHENIX physics program.

Index Terms—Calorimeters, electromagnetic calorimetry, performance evaluation, prototypes, Relativistic Heavy Ion Collider (RHIC), silicon photomultiplier (SiPM), simulation, “Spaghetti” Calorimeter (SPACAL), super Pioneering High Energy Nuclear Interaction eXperiment (sPHENIX)

I. INTRODUCTION

THE super Pioneering High Energy Nuclear Interaction eXperiment (sPHENIX) is a future experiment [1] at the Relativistic Heavy Ion Collider that will elucidate QCD matter and interactions by studying the quark-gluon plasma (QGP) [2]–[6]. The sPHENIX detector is designed to measure the QGP at a variety of length scales using various probes in order to provide insights into the microscopic properties of the QGP. One such probe is jets of correlated particles arising from hard scattering interactions between two partons hadronizing into collimated shower of particles. The energy loss of partons traversing the QGP is of particular interest. Capabilities for heavy flavor measurements in sPHENIX will allow for detailed study of flavor dependent energy loss through measurement of heavy flavor hadrons, as well as heavy flavor jets. To accomplish these measurements, sPHENIX is designed with a tracking system, a calorimeter system with 2π acceptance and pseudorapidity coverage of $|\eta| < 1.1$, and the former BaBar solenoid magnet [7]. The calorimeter system consists of an electromagnetic calorimeter and a hadronic calorimeter. The calorimeter system will allow for the measurement of jets with transverse momentum as low as 10 GeV, as well as provide the first measurements of hadronic jet reconstruction at RHIC.

The sPHENIX electromagnetic calorimeter (EMCal) is a sampling calorimeter designed to measure electrons, positrons and photons. The EMCal has a coverage of $|\eta| < 1.1$ and $0 < \phi < 2\pi$. The EMCal is segmented into *towers* of size $\Delta\eta \times \Delta\phi = 0.024 \times 0.024$ that set the granularity of the calorimeter. The towers are defined within calorimeter *blocks* that consist of scintillating fibers embedded in a mix of tungsten powder and epoxy. Each block corresponds to a 2x2 array

of towers. Each tower is equipped with a lightguide to collect the light from the fibers. The blocks are distributed in 64 sectors that describe an overall cylindrical geometry concentric with the beamline and centered at the interaction point (IP) of the particle collisions. Each hemisphere $0 < |\eta| < 1.1$ has 32 sectors distributed evenly in azimuth. Each sector has 24 rows of blocks that extend along the beamline, and each row has 4 blocks that extend in ϕ . The blocks are tapered in both η and ϕ , resembling a truncated pyramid, and giving a 2D projective geometry. The blocks are further tilted such that the fibers point to a sphere around the interaction point, minimizing channeling and improving energy resolution.

II. PROTOTYPE ELECTROMAGNETIC CALORIMETER

The 2018 EMCal prototype is an array of 8x8 calorimeter towers, or 4x4 blocks, covering a solid angle of $\Delta\eta \times \Delta\phi = 0.2 \times 0.2$ centered at $\eta = 1$. Figure 1 shows a drawing of the EMCal prototype.

A. EMCal Block Production

The EMCal blocks were produced by embedding a matrix of scintillating fibers (SciFi) in a mix of epoxy and tungsten powder (W). The blocks are similar to the “Spaghetti Calorimeter” design used in other experiments [8]–[14]. The scintillating fibers are as long as the block and are distributed uniformly across the block’s cross section. There is a total of 2668 fibers per block. The towers within a block have an area of approximately $(1.1R_M)^2$, where $R_M \sim 2.3$ cm is the Molière radius. The length of the towers varies with η and it has an approximate value of $\sim 20X_0$, where $X_0 \sim 7$ mm is the radiation length. The blocks have a density of approximately 9.5 g/cm³ and a sampling fraction of $\sim 2.3\%$.

The materials used to produce the blocks are listed in Table I along with some of their properties. The blocks were produced at the University of Illinois at Urbana-Champaign following this procedure:

- Scintillating fibers are dropped into mesh screens that hold the fibers in place.
- The fiber-screen assembly is put into a mold.
- Tungsten powder is poured into the mold. The mold is placed on a vibrating table to pack the powder.
- Epoxy is poured into the top of the filled mold, while a vacuum pump is used at the bottom to extract the air as well as pull the epoxy through the mold.
- The filled mold is left to dry until the mix is solid.
- The block is unmolded and machined to its final shape. A diamond tip is used to machine the readout ends of the block.

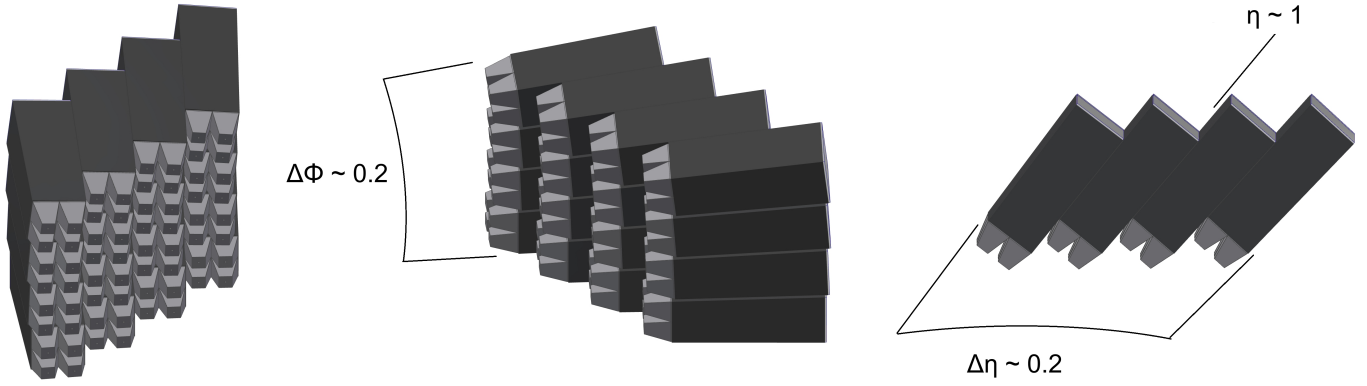


Fig. 1. EMCAL prototype. The prototype consists of an array of 4x4 blocks, covering a solid angle of $\Delta\eta \times \Delta\phi = 0.2 \times 0.2$ centered at $\eta = 1$. Each block (dark gray) corresponds to a 2x2 array of towers defined by lightguides (light gray).

TABLE I
EMCAL BLOCK MATERIALS

Material	Property	Value
Scintillating fiber	Saint Gobain BCF-12	
	diameter	0.47 mm
	core material	polystyrene
	cladding material	acrylic
	cladding	single
	emission peak	435 nm
	decay time	3.2 ns
	attenuation length	≥ 1.6 m
Tungsten powder	THP Technon 100 mesh	
	particle size	25-150 μm
	bulk density (solid)	≥ 18.50 g/cm ³
	tap density (powder)	≥ 10.9 g/cm ³
	purity	$\geq 95.4\%$ W
	impurities (≤ 5 percent)	Fe, Ni, O ₂ , Co, Cr, Cu, Mo
Epoxy	EPO-TEK 301	

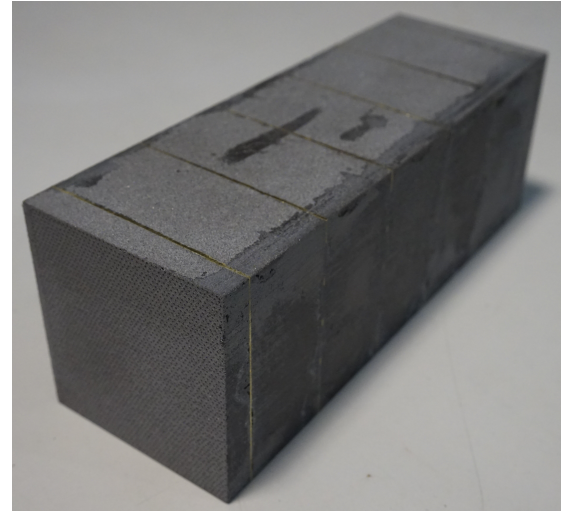


Fig. 2. EMCAL block. The block consists on scintillating fibers embedded in a mix of tungsten powder and epoxy. The blocks are tapered in two dimensions, giving a 2D projective geometry.

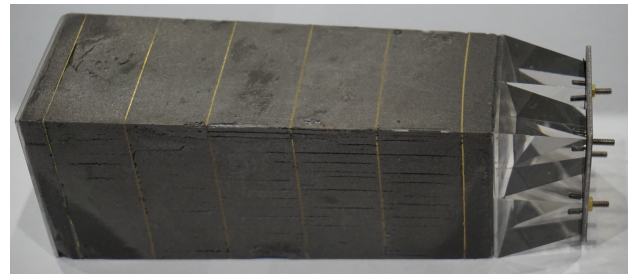


Fig. 3. EMCAL block equipped with lightguides and SiPMs.

98 The finished EMCAL block can be seen in Figure 2. The
 99 quality assurance of the blocks included tests of density, light
 100 transmission and size. The blocks had a density ranging from
 101 9.2 to 9.8 g/cm³, and more than 99% working fibers. The
 102 size of the blocks deviated from the nominal design by less
 103 than 0.02 in.

104 B. Light Collection

105 The light from the scintillating fibers was collected at the
 106 tower's front end (closer to the IP). Lightguides were epoxied
 107 to the front of the towers, while reflectors were epoxied to
 108 the back. The lightguides consisted of UV transmitting acrylic
 109 with a trapezoidal shape (see Figure 3), custom made by NN,
 110 Inc. A silicone adhesive was used to couple each lightguide
 111 to four Silicon photomultipliers (SiPM) Hamamatsu S12572-
 112 33-015P. Each SiPM had 40k pixels distributed evenly in an
 113 area of $15 \times 15 \mu\text{m}^2$, and a detection efficiency of 25%. The
 114 signal per tower was obtained by adding the contribution from
 115 each of the four SiPMs. The signal was read by a preamplifier
 116 and an amplifier, then shaped and driven into a digitizer. More
 117 details about the electronics are given in Section III. Figure 3
 118 shows an EMCAL block equipped with lightguides and SiPMs.

C. Assembly

119 Once the EMCAL blocks were equipped with lightguides and
 120 SiPMs, they were stacked and epoxied together in their final
 121 positions. Since the SiPM signal is sensitive to temperature, a
 122 cooling system was used to remove the heat generated by the
 123 SiPMs and the electronics. The cooling system consisted of
 124 multiple water coils connected to cold plates. The plates were
 125 coupled to the preamplifier boards that follow the SiPMs. Both
 126

127 the cooling system and electronics were controlled remotely.
 128 The EMCal prototype can be seen in Figure 4, which shows the
 129 blocks, lightguides, SiPMs, electronics and part of the cooling
 130 system.

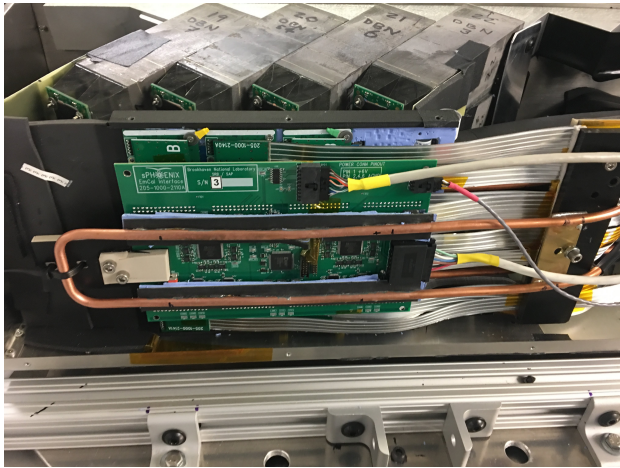


Fig. 4. EMCal prototype showing the SciFi/W blocks, lightguides, SiPMs, electronics and part of the cooling system.

131 III. READOUT ELECTRONICS AND DATA ACQUISITION

132 Light was collected in each tower using four SiPMs. The
 133 SiPMs voltage was set to have a nominal gain of $\sim 2.3 \times 10^5$.
 134 A small thermistor was mounted at the center of the four
 135 SiPMs to monitor the temperature per tower. SiPM signals cor-
 136 responding to one tower were summed, preamplified, amplified
 137 and shaped before going into digitizers. LEDs of 405 nm were
 138 included near the front end of the towers to test the SiPMs
 139 and preamplifier with fixed amplitude pulses. Similarly, charge
 140 injection circuits were included in the amplifiers to provide
 141 fixed amplitude pulses for testing. The EMCal prototype could
 142 operate in a normal gain mode, or a high gain mode with $16 \times$
 143 the normal gain. The gain was selected through a slow control
 144 system.

145 The slow control system consisted of an interface board
 146 connected to a controller board. The interface board was
 147 mounted on the EMCal prototype while the controller board
 148 was in a separate crate. The interface board contained digital-
 149 to-analog converters needed for different testing and moni-
 150 toring tasks. The interface board controlled SiPM bias and
 151 amplifier gain. Testing of preamplifiers and amplifiers was
 152 controlled through the interface board as well. The interface
 153 board also monitored leakage current and local temperature for
 154 compensation. The parameters for these testing and monitoring
 155 tasks were provided to the interface board by the controller
 156 board. An ethernet connection was used to communicate with
 157 the controller board.

158 Signals were digitized following the trigger using a dig-
 159 itization system developed for PHENIX [15]. Signals were
 160 digitized using an analog-to-digital converter (ADC) and Field
 161 Programmable Gate Arrays (FPGA). Signals were collected in
 162 Data Collection Modules (DCM) and data was finally recorded
 163 using the data acquisition system RCDAQ.

164 IV. TEST BEAM

165 The EMCal prototype was tested at the Fermilab Test
 166 Beam Facility as experiment T-1044. The facility provided a
 167 particle beam, detectors such as a lead-glass calorimeter and
 168 a Cherenkov counter, and a motion table (MT6.2C) [16]. The
 169 EMCal was placed in the motion table to allow testing in
 170 different positions with respect to the beam.

171 The particle beam used in the experiment had energies
 172 ranging from 2 to 28 GeV. The beam was composed mainly
 173 of electrons, muons and pions, and their relative abundance
 174 depended on the energy [17], [18]. The beam hit the EMCal
 175 prototype with a frequency of 1 spill per min, where a spill
 176 corresponds to a maximum of $\sim 10^5$ particles during 4s. The
 177 beam had a nominal momentum spread of $\delta p/p \sim 2\%$ for
 178 the energy range used [8], [19], [20]. A lead-glass calorime-
 179 ter was used to measure the accuracy and precision of the
 180 beam momentum. The lead-glass calorimeter had a size of
 181 $45 \times 15 \times 15 \text{ cm}^3$ and a resolution of $(5.6 \pm 0.2)\%/\sqrt{E}$ [21].

182 External detectors were used to discriminate electron signals
 183 from background from minimum ionizing particles (MIPs) and
 184 hadrons. A gaseous Cherenkov counter was placed upstream
 185 of the EMCal to trigger on electron signals. A hodoscope
 186 [8], [9] was placed upstream of the EMCal to determine the
 187 position of the particles in the beam precisely. The hodoscope
 188 consisted of 16 hodoscope fingers (0.5 cm wide scintillators)
 189 arranged in two arrays of 8 fingers each. One array had
 190 the hodoscope fingers arranged vertically and the other array
 191 had them arranged horizontally. The position of a hit in the
 192 hodoscope was given by a horizontal and a vertical hodoscope
 193 finger, with a total of 64 possible positions. Each hodoscope
 194 finger was read out by an SiPM. Four veto detectors were also
 195 placed around the EMCal in order to suppress background
 196 from MIPs. Each veto counter consisted of a scintillator
 197 coupled to a photomultiplier tube (PMT) and read out by a
 198 digitizer.

199 V. SIMULATIONS

200 The EMCal prototype was simulated using GEANT4 [22],
 201 [23] version 4.10.02-patch-02. The physics configuration
 202 QGSP_BERT_HP was used, which is recommended for high
 203 energy simulations. The simulations included an electron beam
 204 of energies 2 to 28 GeV with a Gaussian profile of $\sigma \sim 3.5$
 205 cm. The beam was pointed between Towers 36 and 29, which
 206 are located near the center of the prototype (see Figure 5), fully
 207 covering the towers. In the simulations, the energy deposits
 208 from the electromagnetic showers were converted into light
 209 using Birk's law [24] with constant $k_B = 0.0794 \text{ mm/MeV}$
 210 [25]. The number of photons was converted to number of
 211 fired SiPM pixels taking into account the lightguide collection
 212 efficiency. The number of fired pixels was converted to ADC
 213 counts and then calibrated to energy. To account for SiPM
 214 saturation, the energy was reduced by a factor obtained from
 215 a Monte Carlo simulation of the SiPMs. The simulations were
 216 integrated into the sPHENIX analysis framework.

VI. ANALYSIS METHODS

A. Data Sets

The data sets used in this analysis correspond to a beam of electrons with energies of 2, 3, 4, 6, 8, 12, 16, 20, 24 and 28 GeV. The beam was pointed at either Tower 36 or Tower 29 (see Figure 5). In this paper, whenever Tower 36 or Tower 29 is mentioned, it is referring to the corresponding data set that had the beam centered at either of those towers.

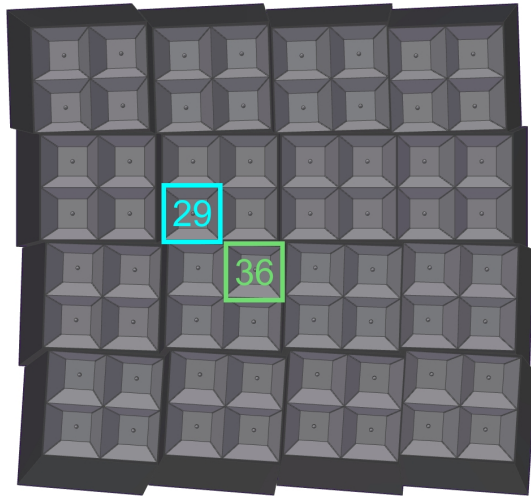


Fig. 5. Front view of the EMCAL prototype showing the towers. Tower 36 (light green) and Tower 29 (light blue) are highlighted.

B. Electron Selection

Different cuts were used in order to suppress background from MIPs and hadrons, and select only events with *good* electrons. For an event to be regarded as a good electron, it had to pass a Cherenkov cut, a vertical and horizontal hodoscope cut, and four veto cuts. For the Cherenkov cut, the energy of the events had to be greater than a threshold of ~ 1500 ADC counts, based on the Cherenkov's energy spectrum. For the vertical and horizontal hodoscope cuts, the events were required to have an energy greater than 50% of the peak energy in the hodoscope's energy spectrum. Only events with one hit in the vertical and one hit in the horizontal hodoscope fingers were considered. For the four veto cuts, the events were required to have an energy less than 20% of the peak energy in the veto's energy spectrum. These cuts gave a number of good electrons of approximately 5000-50000, depending on the energy.

C. Calibration

A preliminary calibration of the data, the *shower calibration*, was done based on how the electromagnetic showers develop within the EMCAL. A uniformity study of the EMCAL prototype showed that the energy measurements vary depending on the position within the EMCAL (see Figure 6). This behavior motivated the use of a secondary energy calibration, the *position dependent correction*. The calibration procedures are as follows:

1) *Shower Calibration*: Calibration constants were applied tower-by-tower to convert the ADC signals to energy. For each event, the energy measured by the EMCAL was obtained as the total energy of a 5x5 cluster of towers around the maximum energy tower. The size of the cluster was selected based on the Molière radius for the EMCAL blocks. A cluster of 5x5 towers contains over 95% of the shower. The energy corresponding to a cluster of 5x5 towers around the tower with the maximum energy is denoted as $E_{cluster}$.

2) *Position dependent correction*: The energy measured by the EMCAL was corrected by a constant that depends on the position of the hit in the EMCAL. Two different corrections were obtained. In the first one, the position was given by a horizontal and a vertical hodoscope finger, for a total of 8x8 possible positions. In the second one, the position was given by the energy averaged cluster position measured by the EMCAL, discretized in 8x8 bins that match the hodoscope. The position dependent calibration constants were obtained from 8 GeV data. For each of the 64 possible positions, a histogram was filled with the cluster energy of the hits in that position. The histogram was then fit with a Gaussian of mean μ . The calibration constant for each position was obtained as $8 \text{ GeV}/\mu$. The position dependent correction changed the energy resolution by 2-3 %, depending on the energy.

3) *Beam Profile Correction*: In the experiment, the beam was collimated and had a different profile at different energies. In addition to the position dependent correction, a *beam profile correction* was introduced in order to correct for the energy dependence of the beam profile. This correction consisted on filling the energy histograms with weights that were obtained by uniforming the distribution of beam particles as a function of position. The beam profile correction changed the energy resolution by 0.1-0.5 %, depending on the energy.

VII. RESULTS AND DISCUSSION

A. Uniformity

Figure 6 shows the cluster energy as a function of position for an input energy of 8 GeV. The results are shown for data and simulations. Figure 6 shows a better energy collection efficiency towards the center of the towers than at the boundaries between blocks and towers.

Figure 7 shows the effect of the position dependent correction on the energy. This figure shows the cluster energy as a function of horizontal hodoscope position. The data is shown before and after the position dependent correction. After the correction is applied, the energy response of the EMCAL becomes more uniform.

B. Linearity and Resolution

Following the analysis procedure described in previous sections, the energy resolution and linearity of the EMCAL prototype was obtained for input energies ranging from 2 to 28 GeV, for both simulations and data.

Figure 8 shows the energy resolution and linearity of the EMCAL prototype using a cut of the size of a tower (approximately $2.5 \times 2.5 \text{ cm}^2$) centered at the tower. The results are shown for data and simulations and include all

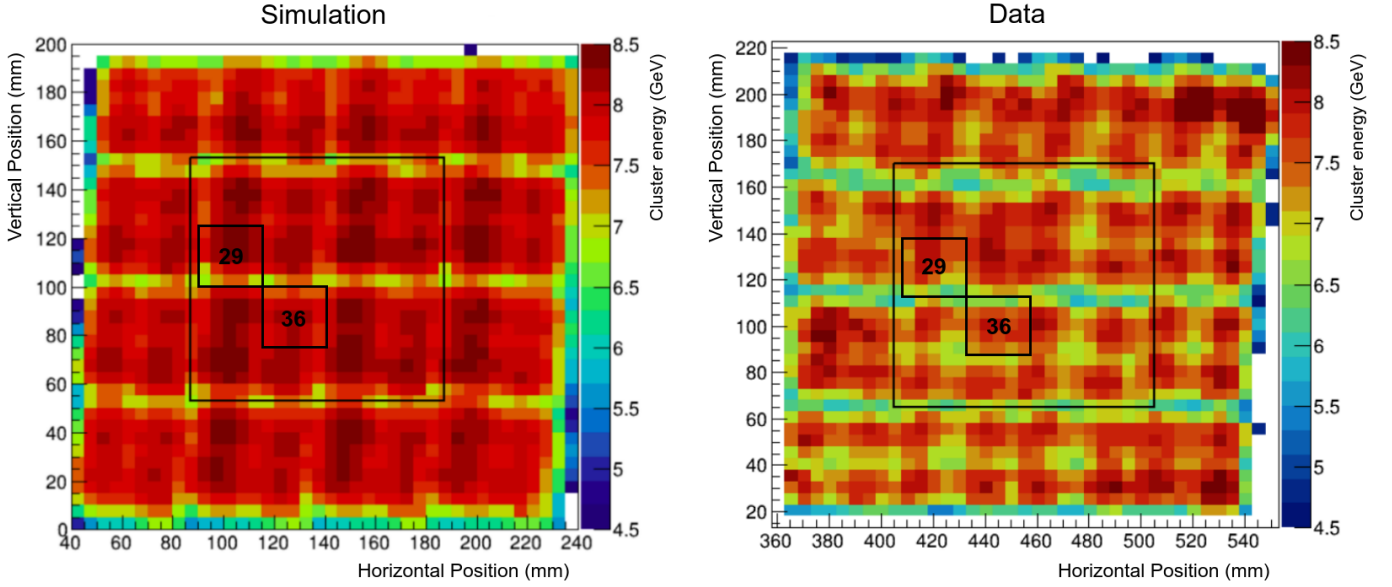


Fig. 6. Cluster energy vs. Position for simulations (left panel) and data (right panel). The results correspond to an input energy of 8 GeV. The central 4x4 towers are shown in big black squares, and the locations of Towers 29 and 36 are shown in small black squares.

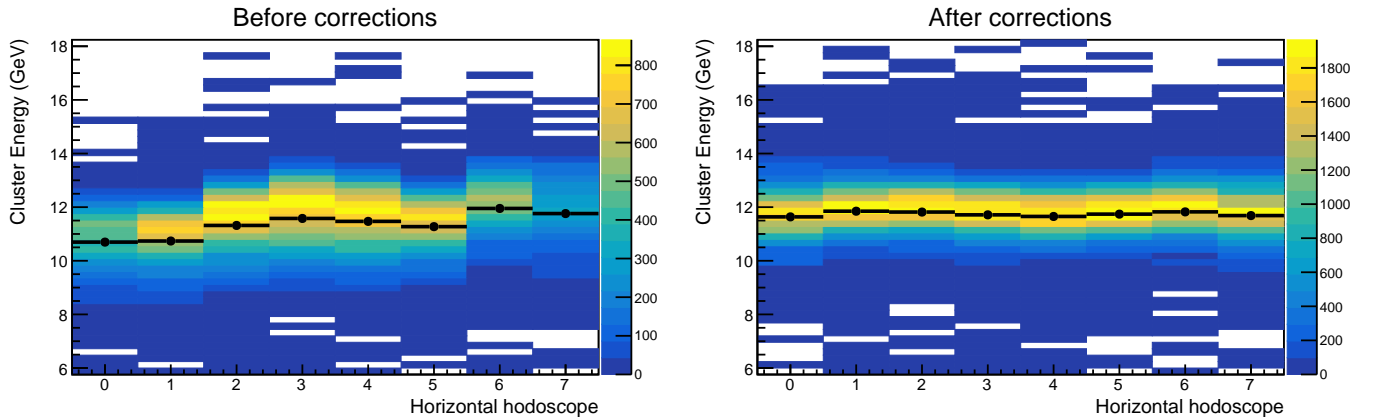


Fig. 7. Cluster energy vs. Horizontal Hodoscope Position before (left panel) and after (right panel) the position dependent correction is applied. The color scale represents the number of events, while the data points correspond to the mean of the energy distributions for each hodoscope position. The data corresponds to a beam of 12 GeV centered at Tower 36.

307 corrections. The error bars in the data points correspond to statistical uncertainties. The linearity was obtained as $E_{cluster} =$
 308 $E_{input} + cE_{input}^2$, where c is a constant. The resolution was
 309 obtained as $\sigma(E_{cluster})/\langle E_{cluster} \rangle = \delta p/p \oplus a \oplus b/\sqrt{E_{input}}$,
 310 where a and b are constants, and a $\delta p/p \sim 2\%$ term was added
 311 to account for the beam momentum spread. Table II shows the
 312 values of the fit constants a, b, c .
 313

314 Figure 8 shows good agreement between towers in terms of
 315 linearity and resolution, for both the hodoscope-based and
 316 cluster-based position dependent corrections. However, the
 317 resolution obtained with the cluster-based correction differs
 318 from the hodoscope-based correction by $\sim 0.6\%$ in the constant
 319 term and $\sim 2.1\%$ in the $1/\sqrt{E}$ term. Since the cluster based
 320 correction depends on the position measured by the EMCal
 321 itself and not the hodoscope, the difference in the results can
 322 come from the position resolution of the EMCal. Additionally,
 323 the energy resolution seems to be better in the simulations than

TABLE II
 EMCAL LINEARITY AND RESOLUTION FOR A $2.5 \times 2.5 \text{ cm}^2$ CUT
 CENTERED ON A TOWER

$$\text{Resolution fit: } \sigma(E_{cluster})/\langle E_{cluster} \rangle = 2\% \oplus a \oplus b/\sqrt{E_{input}}$$

$$\text{Linearity fit: } E_{cluster} = E_{input} + cE_{input}^2$$

	Tower	a	$b \text{ (GeV}^{1/2}\text{)}$	$c \text{ (GeV}^{-1}\text{)}$
Data, hodoscope	36	3.2 ± 0.1	13.8 ± 0.2	$(-9.4 \pm 0.1) \times 10^{-4}$
Data, hodoscope	29	3.8 ± 0.1	12.8 ± 0.2	$(-10.9 \pm 0.1) \times 10^{-4}$
Data, cluster	36	2.7 ± 0.1	15.8 ± 0.3	$(-12.8 \pm 0.1) \times 10^{-4}$
Data, cluster	29	3.2 ± 0.1	14.9 ± 0.3	$(-8.6 \pm 0.1) \times 10^{-4}$
Simulation		2.66 ± 0.02	12.0 ± 0.04	$(-12.7 \pm 0.1) \times 10^{-4}$

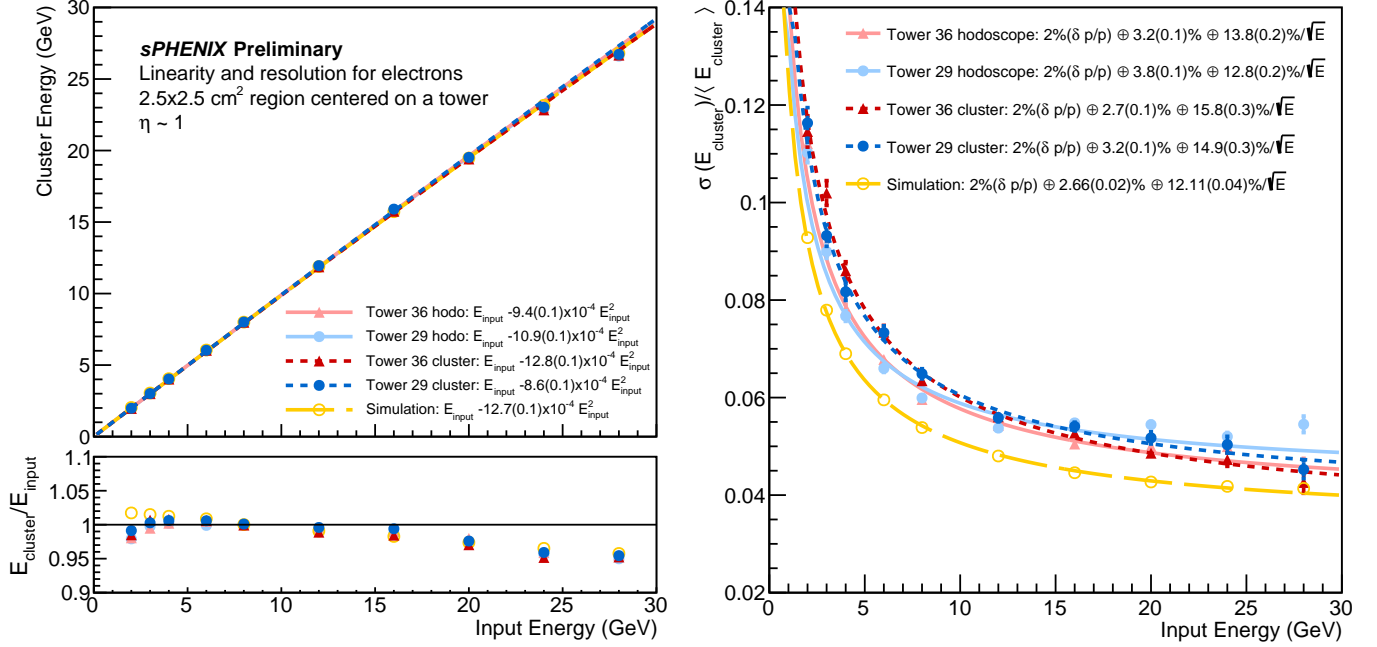


Fig. 8. Linearity and resolution of the EMCal prototype for a $2.5 \times 2.5 \text{ cm}^2$ centered on a tower. The data corresponds to Tower 36 (red and pink triangle points) and Tower 29 (light and dark blue full circles). The data was corrected using the hodoscope-based (solid lines) and cluster-based (fine dashed lines) position dependent corrections. Simulations (yellow open circles, coarse dashed line) are shown for comparison. (top left panel) Cluster energy vs. Input energy. (bottom left panel) $E_{cluster}/E_{input}$ vs. Input Energy. The linearity was obtained as $E_{cluster} = E_{input} + cE_{input}^2$. (right panel) Resolution vs. Input energy. The resolution was obtained as $\sigma(E_{cluster})/\langle E_{cluster} \rangle = \delta p/p \oplus a \oplus b/\sqrt{E_{input}}$, where a $\delta p/p \sim 2\%$ term was added to account for the beam momentum spread.

324 in the hodoscope corrected data by $\sim 0.8\%$ in the constant term
 325 and $\sim 1.2\%$ in the $1/\sqrt{E}$ term. These differences can come
 326 from the lower energy collection at the boundaries between
 327 towers and blocks. The differences in the resolution results
 328 can be minimized by making a cut at the center of the towers
 329 and excluding the boundaries. Figure 9 shows the linearity and
 330 resolution results using a $0.5 \times 1.0 \text{ cm}^2$ cut at the center of the
 331 towers. This figure shows better agreement between data and
 332 simulations. Table III shows the corresponding linearity and
 333 resolution fit constants.

TABLE III

EMCAL LINEARITY AND RESOLUTION FOR A $1.0 \times 0.5 \text{ cm}^2$ CUT AT THE CENTER OF A TOWER

$$\text{Resolution fit: } \sigma(E_{cluster})/\langle E_{cluster} \rangle = 2\% \oplus a \oplus b/\sqrt{E_{input}}$$

$$\text{Linearity fit: } E_{cluster} = E_{input} + cE_{input}^2$$

	Tower	a	$b \text{ (GeV}^{1/2}\text{)}$	$c \text{ (GeV}^{-1}\text{)}$
Data, hodoscope	36	2.4 ± 0.2	12.3 ± 0.5	$(-12.9 \pm 0.3) \times 10^{-4}$
Data, hodoscope	29	2.3 ± 0.2	13.4 ± 0.5	$(+0.7 \pm 0.3) \times 10^{-4}$
Data, cluster	36	2.4 ± 0.2	13.2 ± 0.5	$(-10.9 \pm 0.3) \times 10^{-4}$
Data, cluster	29	2.7 ± 0.2	12.8 ± 0.4	$(-5.9 \pm 0.3) \times 10^{-4}$
Simulation		2.2 ± 0.1	11.6 ± 0.1	$(-11.2 \pm 0.3) \times 10^{-4}$

334 Comparing the 2018 results to the 2016 results of reference
 335 [19], the resolution improved for energies in the range 2 to
 336 8 GeV. In terms of the resolution fit, the $1/\sqrt{E}$ term of
 337 the resolution decreased by $\sim 2.5\%$ and the constant term
 338 increased by $\sim 0.65\%$. Furthermore, linearity improved by
 339 $\sim 1\%$ in the 2018 prototype with respect to the 2016 prototype.

VIII. CONCLUSIONS

340 A prototype of the EMCal was constructed and tested, and
 341 its energy response was studied as a function of position and
 342 energy. The energy resolution and linearity of the EMCal pro-
 343 totype were obtained using two different position dependent
 344 corrections (hodoscope-based and cluster-based) as well as a
 345 beam profile correction. The two data sets used in this analysis
 346 had beam energies ranging from 2 GeV to 28 GeV, but one had
 347 the beam centered at Tower 36 and the other one had the beam
 348 centered at Tower 29. The energy resolution was obtained
 349 for each tower using a cut of $2.5 \times 2.5 \text{ cm}^2$ centered at the
 350 tower. Based on the hodoscope position dependent correction,
 351 the EMCal prototype was found to have a tower averaged
 352 energy resolution of $\sigma(E)/\langle E \rangle = 3.5(0.1) \oplus 13.3(0.2)/\sqrt{E}$.
 353 Based on the cluster position dependent correction, the tower
 354 averaged resolution was found to be $\sigma(E)/\langle E \rangle = 3.0(0.1) \oplus$
 355 $15.4(0.3)/\sqrt{E}$. Both of these results meet the requirements of
 356 the sPHENIX physics program.
 357

REFERENCES

- 358 [1] A. Adare *et al.*, “An Upgrade Proposal from the PHENIX Collabora-
 359 tion,” 2015.
 360

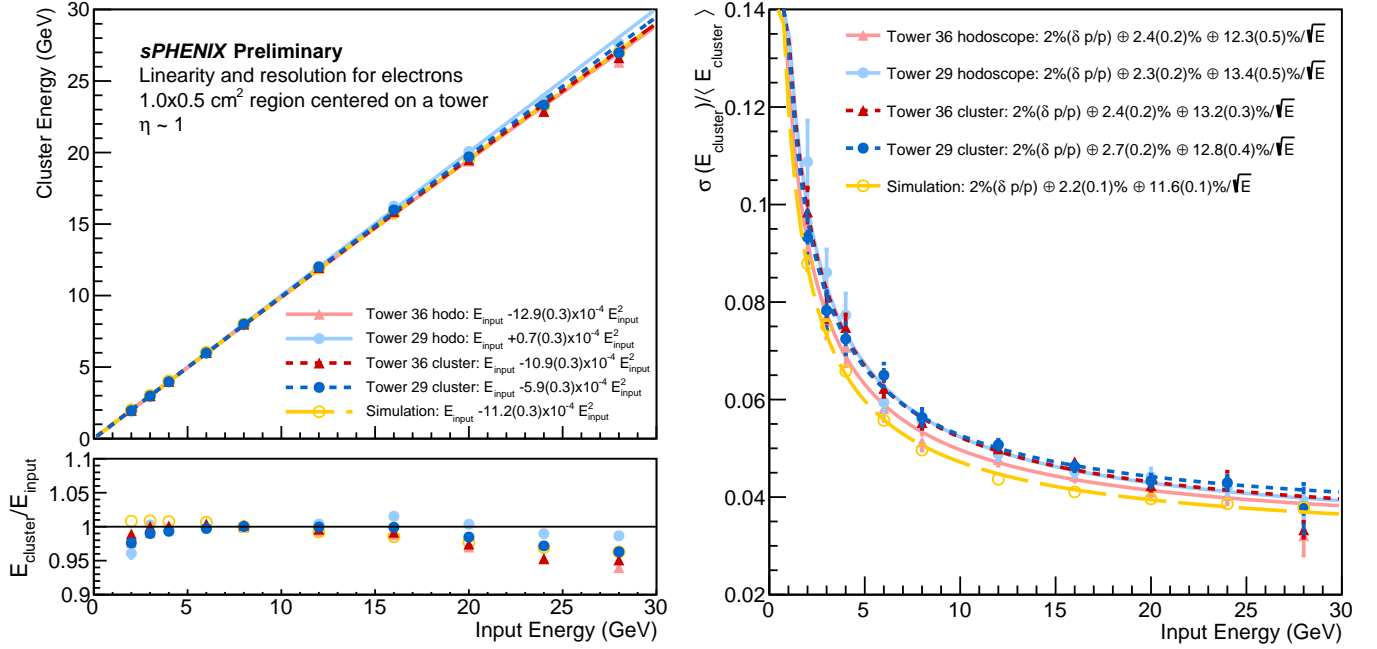


Fig. 9. Linearity and resolution of the EMCal prototype for a $1.0 \times 0.5 \text{ cm}^2$ cut at the center of a tower. The data corresponds to Tower 36 (red and pink triangle points) and Tower 29 (light and dark blue full circles). The data was corrected using the hodoscope-based (solid lines) and cluster-based (fine dashed lines) position dependent corrections. Simulations (yellow open circles, coarse dashed line) are shown for comparison. (top left panel) Cluster energy vs. Input energy. (bottom left panel) $E_{\text{cluster}}/E_{\text{input}}$ vs. Input Energy. The linearity was obtained as $E_{\text{cluster}} = E_{\text{input}} + cE_{\text{input}}^2$. (right panel) Resolution vs. Input energy. The resolution was obtained as $\sigma(E_{\text{cluster}})/\langle E_{\text{cluster}} \rangle = \delta p/p \oplus a \oplus b/\sqrt{E_{\text{input}}}$, where a $\delta p/p \sim 2\%$ term was added to account for the beam momentum spread.

- 361 [2] E.-C. Aschenauer *et al.*, “The RHIC Cold QCD Plan for 2017 to 2023: A Portal to the EIC,” 2016.
- 362
- 363 [3] K. Adcox *et al.*, “Formation of dense partonic matter in relativistic nucleus nucleus collisions at RHIC: experimental evaluation by the PHENIX collaboration,” *Nucl. Phys.*, vol. A757, pp. 184–283, 2005.
- 364
- 365 [4] J. Adams *et al.*, “Experimental and theoretical challenges in the search for the quark gluon plasma: the STAR collaboration’s critical assessment of the evidence from RHIC collisions,” *Nucl. Phys.*, vol. A757, pp. 102–183, 2005.
- 366
- 367 [5] B. B. Back *et al.*, “The PHOBOS perspective on discoveries at RHIC,” *Nucl. Phys.*, vol. A757, pp. 28–101, 2005.
- 368
- 369 [6] I. Arsene *et al.*, “Quark gluon plasma and color glass condensate at RHIC? The perspective from the BRAHMS experiment,” *Nucl. Phys.*, vol. A757, pp. 1–27, 2005.
- 370
- 371 [7] T. G. O’Connor *et al.*, “Design and testing of the 1.5 T superconducting solenoid for the BaBar detector at PEP-II in SLAC,” *IEEE Trans. Appl. Supercond.*, vol. 9, pp. 847–851, 1999.
- 372
- 373 [8] O. Tsai, L. Dunkelberger, C. Gagliardi, S. Heppelmann, H. Huang *et al.*, “Results of R&D on a new construction technique for W/ScFi Calorimeters,” *J. Phys. Conf. Ser.*, vol. 404, p. 012023, 2012.
- 374
- 375 [9] O. D. Tsai *et al.*, “Development of a forward calorimeter system for the STAR experiment,” *J. Phys. Conf. Ser.*, vol. 587, no. 1, p. 012053, 2015.
- 376
- 377 [10] B. D. Leverington *et al.*, “Performance of the prototype module of the GlueX electromagnetic barrel calorimeter,” *Nucl. Instrum. Meth.*, vol. A596, pp. 327–337, 2008.
- 378
- 379 [11] S. A. Sedykh *et al.*, “Electromagnetic calorimeters for the BNL muon (g-2) experiment,” *Nucl. Instrum. Meth.*, vol. A455, pp. 346–360, 2000.
- 380
- 381 [12] T. Armstrong *et al.*, “The E864 lead-scintillating fiber hadronic calorimeter,” *Nucl. Instrum. Meth.*, vol. A406, pp. 227–258, 1998.
- 382
- 383 [13] R. D. Appuhn *et al.*, “The H1 lead / scintillating fiber calorimeter,” *Nucl. Instrum. Meth.*, vol. A386, pp. 397–408, 1997.
- 384
- 385 [14] D. W. Hertzog, P. T. Debevec, R. A. Eisenstein, M. A. Graham, S. A. Hughes, P. E. Reimer, and R. L. Tayloe, “A high resolution lead scintillating fiber electromagnetic calorimeter,” *Nucl. Instrum. Meth.*, vol. A294, pp. 446–458, 1990.
- 386
- 387 [15] W. Anderson *et al.*, “Design, Construction, Operation and Performance of a Hadron Blind Detector for the PHENIX Experiment,” *Nucl. Instrum. Meth.*, vol. A646, p. 35, 2011.
- 388
- 389 [16] The Fermilab test beam facility. accessed: Apr 5, 2017. [Online]. Available: <http://ftbf.fnal.gov>
- 390
- 391 [17] N. Feege, “Low-energetic hadron interactions in a highly granular calorimeter,” Ph.D. dissertation, Physics Department, Hamburg U., 2011. [Online]. Available: <http://www-library.desy.de/cgi-bin/showprep.pl?thesis11-048>
- 392
- 393 [18] M. Blatnik *et al.*, “Performance of a Quintuple-GEM Based RICH Detector Prototype,” *IEEE Trans. Nucl. Sci.*, vol. 62, no. 6, pp. 3256–3264, 2015.
- 394
- 395 [19] C. A. Aidala *et al.*, “Design and Beam Test Results for the sPHENIX Electromagnetic and Hadronic Calorimeter Prototypes,” *IEEE Trans. Nucl. Sci.*, vol. 65, no. 12, pp. 2901–2919, 2018.
- 396
- 397 [20] M. Backfish, “Meson test beam momentum selection,” <http://beamdocs.fnal.gov/AD/DocDB/0048/004831/004/DPOverP.pdf>, 2016.
- 398
- 399 [21] R. M. Brown, W. M. Evans, C. N. P. Gee, P. W. Jeffreys, G. N. Patrick, M. D. Rousseau, B. J. Saunders, and M. Sproston, “An Electromagnetic Calorimeter for Use in a Strong Magnetic Field at LEP Based on Ceren 25 Lead Glass and Vacuum Phototriodes,” *IEEE Trans. Nucl. Sci.*, vol. 32, pp. 736–740, 1985.
- 400
- 401 [22] S. Agostinelli *et al.*, “GEANT4: A Simulation toolkit,” *Nucl. Instrum. Meth.*, vol. A506, pp. 250–303, 2003.
- 402
- 403 [23] J. Allison *et al.*, “Geant4 developments and applications,” *IEEE Trans. Nucl. Sci.*, vol. 53, p. 270, 2006.
- 404
- 405 [24] J. B. Birks, “Scintillations from Organic Crystals: Specific Fluorescence and Relative Response to Different Radiations,” *Proc. Phys. Soc.*, vol. A64, pp. 874–877, 1951.
- 406
- 407 [25] M. Hirschberg, R. Beckmann, U. Brandenburg, H. Brueckmann, and K. Wick, “Precise measurement of Birks k_B parameter in plastic scintillators,” *IEEE Trans. Nucl. Sci.*, vol. 39, pp. 511–514, 1992.
- 408
- 409
- 410
- 411
- 412
- 413
- 414
- 415
- 416
- 417
- 418
- 419
- 420
- 421
- 422
- 423
- 424
- 425
- 426
- 427
- 428